





Plasma formation with regulated electric potential distribution in SMOLA helical mirror device

Viktor O. Ustyuzhanin^{1,2} , Ivan A. Ivanov¹ , Anna A. Inzhevatkina¹  and Anton V. Sudnikov¹ 

¹Budker Institute of Nuclear Physics, Novosibirsk, Russia

²Novosibirsk State University, Novosibirsk, Russia

Corresponding author: Viktor O. Ustyuzhanin, V.O.Ustyuzhanin@inp.nsk.su

(Received 30 May 2025; revision received 28 July 2025; accepted 10 August 2025)

This paper presents experimental results from the SMOLA device, constructed at the Budker Institute of Nuclear Physics, to verify the concept of helical mirror confinement. The experiments discussed focus on collision regimes and plasma rotation in the transport section, controlled primarily by the axisymmetric plasma gun. The plasma gun of the SMOLA comprises a lanthanum hexaboride cathode, a hollow copper anode and magnetic coils, forming a magnetron discharge with a high degree of ionisation and a radial electric field for $\mathbf{E} \times \mathbf{B}$ drift. Ion collisionality is adjustable from collisional to collisionless via magnetic configuration and gas feed of the plasma gun. The main processes in collisions are the ion–ion binary collisions. Electric potential radial distribution, governed by discharge voltage, the anode geometry and its potential, enables $\mathbf{E} \times \mathbf{B}$ plasma rotation such that the axial magnetic mirrors velocity in the rotating plasma reference frame can be comparable to the ion thermal velocity ($V_Z \geq V_{Ti}$), which realises conditions for effective plasma confinement.

Key words: plasma devices, plasma confinement, electric discharges

1. Introduction

Open magnetic systems significantly vary in design and operating principles. Theoretically, they enable the use of non-tritium and neutron-free reactions, which prolongs operational lifespans without costly reconstructions (Anikeev *et al.* 2015; Gota *et al.* 2019). To date, several projects using magnetic mirror devices for fusion with different methods of achieving good energy confinement, macroscopic and kinetic stability have been proposed (see, for example, Gota *et al.* 2019; Yakovlev *et al.* 2022; Jäderberg *et al.* 2023; Forest *et al.* 2024). Among them, the Gas-Dynamic Multiple-mirror Trap (GDMT) project was proposed in Budker INP (Postupaev *et al.* 2017; Skovorodin *et al.* 2023). This modular concept involves a central gas-dynamic cell and separate multiple-mirror sections for improved axial confinement. The existing method of multiple mirror suppression of axial heat flux in

combination with a gas-dynamic central cell can provide an effective mirror ratio of approximately 100. One of the new options for multiple-mirror plasma confinement is the concept of helicoidal field confinement (Beklemishev 2013).

In this concept, a stationary magnetic field with helical symmetry is used for creation of magnetic mirrors moving axial in the $\mathbf{E} \times \mathbf{B}$ rotating plasma reference frame. In a helical mirror system, a required spatial profile of the radial electric field can be set by proper biasing of endplates and limiters. This allows the direct control of the $\mathbf{E} \times \mathbf{B}$ plasma rotation. Also, depending on the direction of the magnetic corrugation motion relative to the plasma flow, the force acting on the particles leads either to the deceleration of the plasma and its transfer back to the central cell of the trap, or to the acceleration of the plasma jet (Beklemishev 2015). Theoretical calculations (Beklemishev 2016; Chernoshtanov & Ayupov 2021) predict that the plasma confinement time will exponentially depend on the length of the magnetic system, which is much more efficient than in other open magnetic configurations: linear dependence (mirror cell), quadratic (multi-mirror trap). Moreover, Beklemishev (2016) predicted radial plasma expansion if the plasma axis is charged positively (including the case of the rotation in ambipolar electric field) and radial plasma contraction if the plasma axis is charged negatively.

To verify the concept of helical confinement, the SMOLA device was created in the Budker Institute of Nuclear Physics of the Russian Academy of Science (BINP SB RAS) in 2017 (Postupaev *et al.* 2017; Sudnikov *et al.* 2017). The suppression of the axial plasma flow by the helical section has also been demonstrated (Sudnikov *et al.* 2019). An improvement in the confinement was observed with an increase in the magnetic field, the corrugation ratio and the plasma rotation velocity (Sudnikov *et al.* 2020). The increase in plasma density in the entrance trap by a factor of 1.6 in helical configuration was achieved (Sudnikov *et al.* 2022a). The effect strongly depends on the direction of the plasma rotation (Sudnikov *et al.* 2022b).

The SMOLA device consists of an input expander (confinement zone, CZ) with a discharge-forming system (plasma source), figure 1, transport section (TS) with helical and straight solenoids for decelerating or accelerating the plasma flow depending on the direction of plasma rotation, and exit expander with a radial segmented endplate. The axisymmetric field in the transport section is $B_{\max} = 0.04 \div 0.15$ T with the tuneable average mirror ratio along the magnetic field line $R_{\text{mean}} = 12.5$. The radial electric field reaches up to $E_r \sim 3$ kV m⁻¹ and is created by longitudinal plasma conductivity from the cathode biasing of the plasma source.

There are two aims in the helical confinement investigation for the GDMT project: selection of the collision regime in the region with helical magnetic field and plasma rotation control in the device. The effective case for confinement in the mirror device includes only the ions' Coulomb collisions in the collisional regime and the ions' anomalous scattering in the collisionless regime. In the rotating reference frame, the axial magnetic mirror velocity V_Z , defined through angular plasma rotation velocity $V_Z = h\omega_{E \times B}/2\pi = hcE_r/2\pi aB_z$ (h is the helicity period, a is the plasma radius, E_r is the radial electric field and B_z is the longitudinal magnetic field) should correlate with ion thermal velocity so that $V_Z \geq V_{Ti}$. If $V_z \ll V_{Ti}$, the force pumping the plasma seems to be weak; in the case where $V_z \gg V_{Ti}$, it is too difficult to populate trapped ions. All these characteristics are functions of plasma parameters such as density, temperature and electric field which can be first set by a plasma forming system.

The plasma discharge system in the SMOLA device is an axisymmetric system with hot LaB₆ cathode using a magnetically insulated discharge in a magnetron configuration. The plasma source is based on a similar discharge configuration as

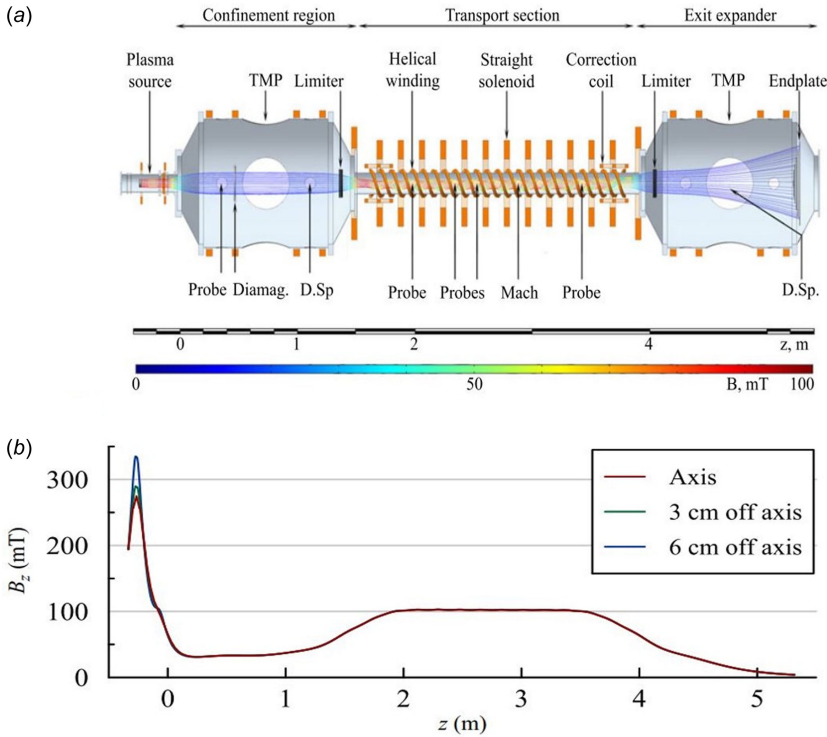


FIGURE 1. SMOLA device configuration. Positions of the diagnostics are indicated. Here, z is the axial coordinate measured from the plasma source exit. (a) Layout of the SMOLA helical mirror. (b) Axial magnetic field distribution.

described by Akhmetov *et al.* (2016) and Kreter *et al.* (2017) for ion sources and PSI-research. Such a type of source realises stationary plasma flow (the discharge duration can be more than 100 ms) with a density up to 10^{19} m^{-3} , high ionisation degree (more than 50 %) and radial electric field necessary for $\mathbf{E} \times \mathbf{B}$ drift with rotation velocity $\omega = (0.5 \div 1) \times 10^6 \text{ s}^{-1}$ in SMOLA (Ivanov *et al.* 2021). This source configuration operates without additional impedance matching systems compared with RF-driven plasma sources. Moreover, arc sources with cold cathodes require more discharge power for comparable plasma parameters.

This paper investigates plasma source control of collisionality and radial electric field distribution for effective confinement in the SMOLA helical magnetic mirror device.

2. Experimental set-up

2.1. Plasma gun layout

The plasma source is an axisymmetric system with planar circular hot cathode based on LaB_6 , a hollow copper anode, two main magnetic coils and a vacuum chamber 14 cm in diameter and 48 cm in length (Ivanov *et al.* 2021). Figure 2 shows a layout of the plasma source with sketchy feeding diagram. LaB_6 , as a cathode material, offers several advantages: it remains reusable even after exposure to air or water leaks. It does not have to be recoated when the machine is exposed to

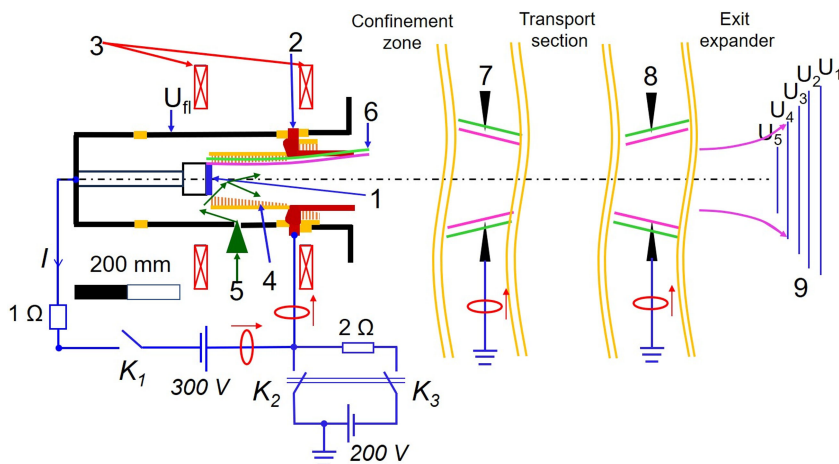


FIGURE 2. Plasma source geometry with main power supply diagram. 1, LaB₆ cathode; 2, copper anode; 3, magnetic field coils; 4, floating diaphragms; 5, gas feeding system; 6, magnetic field lines; 7, limiter in entrance of the transport section; 8, limiter after the transport section; 9, radial segmented plasma endplate; K₁, K₂ and K₃, the IGBT transistors; the red rings, Hall probes.

air. The material can withstand the higher ion fluxes associated with higher current discharges. The cathode is a circular disc of sintered LaB₆ powder with diameter $D = 5$ cm and thickness $h = 3$ mm. It is indirectly heated by the radiation of a tungsten spiral, which is located behind the cathode (such as the tungsten spiral described by Goebel, Hirooka & Sketchley 1985). The spiral heats the cathode up to $T = 1900$ K. The heater current is supplied via an insulated feeder at the cathode flange centre and completes the circuit on the vacuum side. A power of $N = 800$ W is required to heat the cathode up to the operating temperature.

The copper anode was grounded in the start operation mode (the short anode mode, SA mode, Sudnikov *et al.* 2020; Ivanov *et al.* 2021; Sudnikov *et al.* 2022a, b) because there was weak electrical conductivity between the anode and plasma. An anode potential control relative to the grounded SMOLA device appeared after its geometry change. The anode was extended along the device axis to increase the electric contact surface between the anode and plasma flow (the anode was lengthened from 2 to 7 cm to improve this contact, see dark red long triangle in figure 2); additionally, the elongation of the anode was greater than its aperture diameter, which led to effective plasma parameter regulation by varying of the anode–cathode magnetic insulation. So, currently, there are two experimental modes of the plasma gun: the grounded anode and the biased anode with regulated electric switches. Anode–cathode isolation (or the anode magnetic insulation) is created by a longitudinal magnetic field so the magnetic field line starting on the edge of the cathode (pink line in figure 2) usually touches the anode’s exit in standard magnetic configuration. In the operating mode, the anode is projected to the central limiter’s diaphragm at the confinement region through magnetic lines (green line in figure 2, the limiters are grounded) while the cathode is projected to the second plate of the plasma dump at the exit expander.

The gun’s magnetic field is created by two coils placed coplanarly to the cathode and the anode correspondingly. They are fed independently, so it allows for

the required magnetic insulation and gun magnetic mirror ratio to be created with respect to the entrance expander of the device. In the discussed experiments, the mirrors of this trap were asymmetric with mirror ratios $R \approx 8$ on the plasma source side and $R \approx 3$ on the helical mirror side. In the paper, we define the anode magnetic insulation as cathode–anode magnetic field relation B_c/B_a . The magnetic field in the cathode and the anode position is calculated from current measurements from the coils by Hall probes. We used values of the magnetic field at the z -location of the anode and cathode. In typical experiments with the SA mode, $B_c/B_a = 2.67$, and $B_c/B_a = 1.34$ in the LA mode.

The volume between the cathode and the anode is limited by floating molybdenum diaphragms (FDs) in the source (Ivanov *et al.* 2021). The diaphragms are placed in a ceramic box to isolate them from the source's walls. This system was located in the interelectrode area of the gun to reduce the amount of puffing gas in the source and increase the gas efficiency of the gun.

The electric feeding of the plasma gun is carried out by a capacitor through the IGBT transistor (K_1) and resistive ballast. The inductive impedance of feeders is negligible in relation to the ballast. The feeding capacitor consists of a series of supercapacitors with a total capacity of 10 F. It is charged up from -150 V to -300 V. The cathode is connected to the second plate of the exit plasma endplate through a resistance of 0.2Ω . All plates of the pumper are powered by DC sources in 50 V steps,

$$U_k = -k \cdot U, \quad (2.1)$$

where $k = 1, 2, \dots, 5$ is the plate number and $U = 50$ V (figure 2, see number 9 in the exit expander).

The anode potential (relative the grounded device) is regulated independently of the anode–cathode voltage in the plasma source. It is charged up from -200 V to 200 V. Two IGBT transistors in the anode circuit (K_2 and K_3) allow for the anode potential to be changed (from grounded to positive or negative, and back) during the experimental pulse.

The gas feeding of the plasma gun is carried out by two independent gas valves. The first serves for the fast filling of the gun volume and is open only for the first 310 ms with the discharge initiation and begins gas puffing simultaneously with the switching on of the cathode voltage. The amount of puffed hydrogen atoms is close to 10^{21} . The second works during the whole plasma discharge and carries out the stationary gas feeding through the thin long capillary for dumping the pulsations and smoothing out of the gas flow. The H_2 gas puff rate is within approximately 10^{19} – 10^{20} atoms s^{-1} (typical $J_{H_2} \approx 10^{21}$ atoms $s^{-1} \approx 60$ eq.A) and is regulated by the working gas pressure on the high-pressure side of the valve. It lies within the limits of 10^{-1} – 2 bar.

The typical experimental diagrams are shown in figure 3. First, the cathode heating switches off because the Ampere force of the current in the tungsten spiral in the external magnetic field of the gun can break the heater. Then, the confining magnetic field is switched on. It is created by different axial coils powered by the supercapacitors with corresponding voltages. When the current in the coils reaches the stationary phase, the fast gas valve opens and the cathode potential is switched on. This time corresponds to $t = 0$ ms on the diagram. The stationary plasma discharge builds up during the first 4060 ms. Average values on the flattop of the discharge ($t \leq 120$ – 180 ms) are used to plot radial profiles of the plasma parameters.

The experimental results of the research correspond to different regimes of the plasma source: the short anode mode (SA) with (and without) floating diaphragms

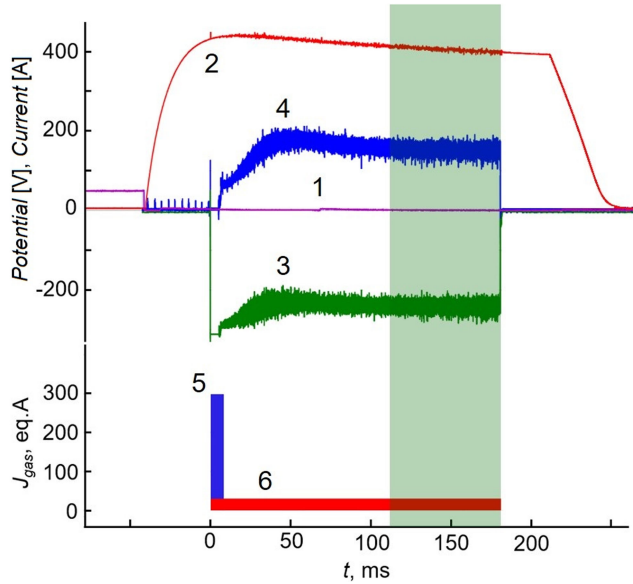


FIGURE 3. Typical plasma pulse in the SMOLA device. 1, cathode heating; 2, current in the magnetic coils; 3, cathode potential; 4, full discharge current; 5, fast gas valve; 6, slow gas valve. Green area corresponds to the stationary phase of the discharge for probe measurements.

and the long anode mode (LA) with floating diaphragms. All the following experiments were performed in the straight field regime of the SMOLA device without a helical field.

2.2. Diagnostics

The following diagnostics were actively used in the described experiments. Radially movable sets of electrostatic probes were installed in the confinement region ($z = 0.4$ m), in the transport section at $z = 2.04$ m (second corrugation period). Each set includes a double probe and two radially shifted emissive probes. Double probes at $z = 0.4, 2.04$ m measure IV characteristic. The emissive probes with thoriated tungsten wires were heated by the plasma during 50 milliseconds at the initial part of the discharge, and then provided simultaneous measurements of plasma potential and radial electric field. The reach of the probe working temperature was verified by thermal radiation of the wire. The emissive probe reaches working temperature during $t \leq 40$ ms at radial coordinates $r \leq 60$ mm. At the outer region ($r = 6080$ mm), the heating duration is $t = 90$ ms. The temperature rise time is consistent with the estimations of Hershkowitz *et al.* (1983). At $t = 185$ ms, the plasma source is turned off to avoid damaging the probes.

An imaging Doppler spectrometer in the confinement zone ($z = 1.15$ m) was used to monitor plasma rotation (Inzhevatkina *et al.* 2021) that can compare with the emissive probe's electric field measurements. The spectrometers also provide the ion temperature measurement due to the Doppler broadening of the emission spectral line of the charge-exchanged hydrogen.

Hall probes measured the currents from electrodes (cathode, anode, central diaphragms in each limiter, and plates of plasma endplate) to plasma and back

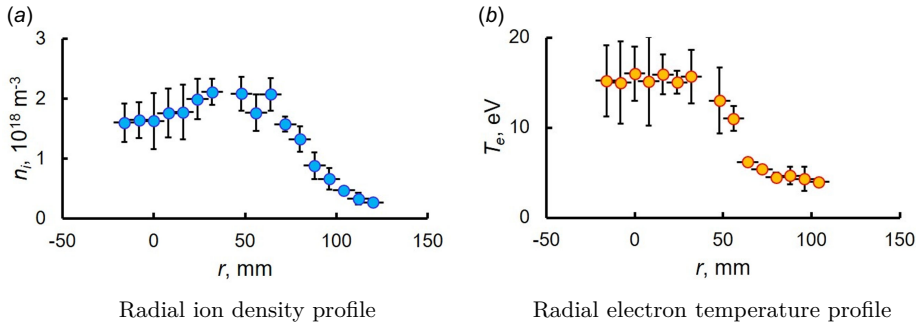


FIGURE 4. Typical radial distribution of the plasma parameters in the confinement zone. Power of the discharge 40 kW, $J_{\text{gas}} = 40$ eq.A, $B_c/B_a = 2.67$. Data are measured by the double probe at $z = 0.4$ m.

in the SMOLA device. Hall probes were located on each electrode (figure 2, red rings).

Gas measurements were realised by ionisation vacuum gauges in the confinement zone ($z = 0.4$ m), in the transport section at $z = 2.76$ m (sixth corrugation period) and the exit expander ($z = 4.34$ m). The gas pressures temporal dynamics can be used for gas density measurements to estimate plasma gas balance and collisional scale (note that all ionisation vacuum gauges have doubtful accuracy owing to the plasma ultraviolet emission: we shielded them from direct radiation to minimise this effect, but an accurate gas pressure estimation can only be made just after plasma disappearance).

We assumed that the radial distributions of plasma parameters are axially symmetric and that the radial displacement of the plasma axis is negligible compared with the plasma radius for all operating regimes. The first assumption relies on the axially symmetric configuration of the plasma source, confinement region and transport section in the straight field regime. The second one is set by the correction magnetic coils in the entrance and exit of the transport section.

The experimental data were obtained in the following way. We made approximately 20 identical experimental discharges in each configuration. Probe sets were moved radially between discharges.

3. Plasma density and ion collisionality

Sample radial distributions of the plasma density and electron temperature, measured by the double probes, are shown in figure 4. The vertical error bars in the graphs correspond to the error of the I-V curve fitting and the horizontal error bars correspond to the probe dimensions (the probe's length is 6 mm for the unit fitted at $z = 0.40$ m and 4 mm for all other units). Ion density radial distribution has a tubular form similar to that illustrated in early versions of such a type of gun (Kreter *et al.* 2017; Akhmetov *et al.* 2019). The position $r^* = 50\text{--}60$ mm of the plasma radius corresponds to intersection of the plasma gun electrode's magnetic surfaces. The density difference between the plasma centre $r = 0$ and point r^* corresponds to approximately 30 %. The main parameters controlled by the plasma gun that can regulate ion collisions conditions are discharge power supply (cathode-anode voltage), amount of the gas feed and the anode magnetic insulation.

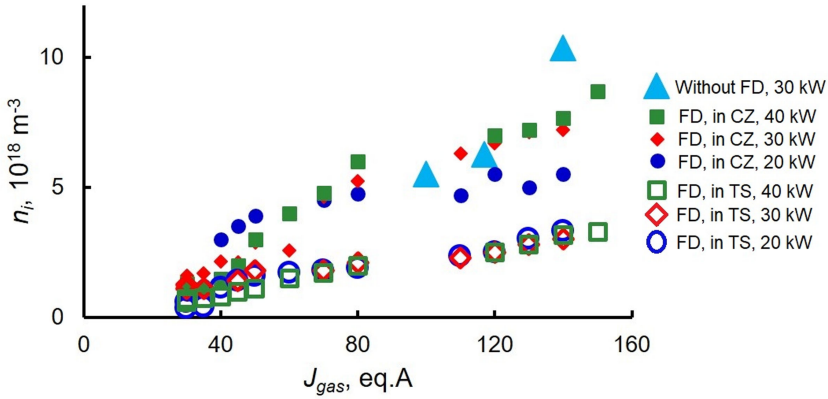


FIGURE 5. Plasma density relation with puffing gas in the CZ ($z = 0.4$ m) and the TS ($z = 2.04$ m) at different discharge power. Density is measured on the axis.

The floating diaphragms installation changed gas conditions in the confinement zone. Plasma density relation with puffing gas flow in the SA mode is demonstrated in figure 5. The plasma source was able to generate a plasma discharge at smaller amount of the puffing gas. In the start experimental series (without FD in the gun with the SA mode), the source could work only with high gas feed $J_{\text{gas}} \geq 100$ eq.A (figure 5, blue triangles). Over the entire range of gas feeding at discharge power higher than 30 kW, a linear dependence of ion density was realised. Such changes of the density's behaviour testify to the high gas efficiency of the plasma source after the FD installation. Plasma density saturation at the gas feed is observed at smaller than 30 kW discharge power and $J_{\text{gas}} \geq 60$ eq.A. The electron temperature reaches $T_e \approx 20$ eV at small gas feed ($J_{\text{gas}} \leq 50$ eq.A). The average ion temperature in the confinement zone at the axis is $T_i = 7 \pm 1$ eV.

Similar plasma density gas feed linear dependence is observed in the transport section at all gas feeding ranges and any power supply (figure 5, black dots). The density in the entrance region of the transport section was roughly three times lower than in the confinement zone at $J_{\text{gas}} \geq 50$ –60 eq.A, giving $n_i = (1 \div 3) \times 10^{18} \text{ m}^{-3}$ (figure 5). The density is comparable in both sections at small gas feed. These results repeated in the LA mode. So the plasma source with FD and both anodes can work with smaller gas density compared with the start experimental mode without FD in the gun.

The magnetic field configuration in the source also affects the plasma parameters in the confinement region (figure 6). The anode magnetic field descension leads to plasma density reduction and neutral gas density increasing. Thus, gas efficiency of the plasma gun can be regulated by the cathode–anode magnetic insulation. Such a regime of the gas efficiency is repeated in the LA mode. In addition, the source's magnetic configuration affects the form of the radial density profile (figure 6a): the density radial distribution becomes more uniform in the plasma centre (the density difference is approximately 15 % at $r \leq r^*$, $B_c/B_a = 2.06$ in the SA mode).

Estimation of the ion collision mode in the transport section depends on the plasma parameters (density and temperature). Values of the measured plasma characteristics in the transport section correspond to the mean free path of an ion with respect to the binary collisions $\lambda_i = 0.5$ –3 m owing to the corresponding equations:

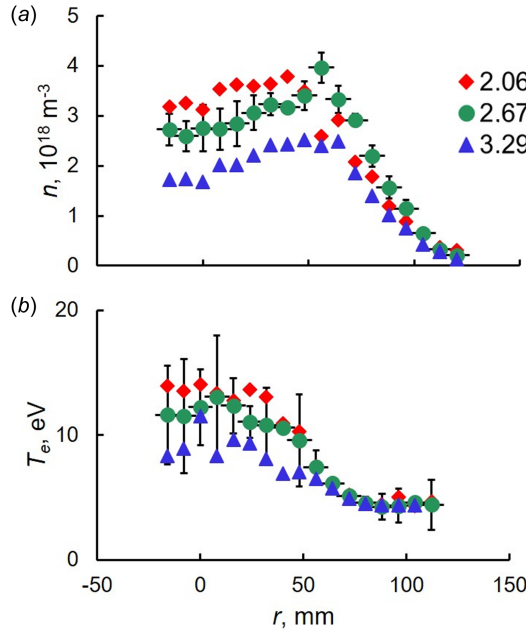


FIGURE 6. Radial profiles of the ion density and the electron temperature at different cathode–anode magnetic field relation (the anode magnetic insulation) at constant gas feeding and power supply in the confinement zone ($z = 0.4$ m). (a) Ion density profile, (b) electron density profile.

$$\lambda_i = \frac{V_{Ti}(T_i)}{v_{ii}(n_i, T_i)}, \quad (3.1)$$

$$V_{Ti} = 9.79 \times 10^5 T_i^{1/2}, \quad (3.2)$$

$$v_{ii}(n_i, T_i) = 4.8 \times 10^{-8} Z^4 n_i T_i^{-3/2} \ln \Lambda. \quad (3.3)$$

The mean free path can be compared with the period of the helical corrugation $h = 0.18$ m as the ratio (we call it dimensionless collisionality ν^*):

$$\nu^* = \frac{h}{\lambda_i}. \quad (3.4)$$

Therefore, the ratio of the mean free path to the period of the helical corrugation was $\lambda/h \sim 0.3$ on the high density bound (in most high-density cases, $\lambda \approx 3h$) and $\lambda/h \sim N$ (N , number of helical corrugation steps in the transport section) on the low density bound (figure 7).

Thus, the plasma source with floating diaphragms and both anode modes can generate plasma flow with a controlled ion collision regime in the transport section with respect to the binary collisions from collisional to collisionless. The anode geometry (SA and LA) does not change the ion collisions mode.

It is very important to compare ion binary collisions with other reactions in the plasma first of all ion charge exchange reactions with a neutral gas. The scale of this reaction is necessary for an estimate of the helical plasma confinement efficiency. The plasma source (after installation of the floating diaphragms) can work with reduced neutral gas density in the SMOLA device, as mentioned previously. This

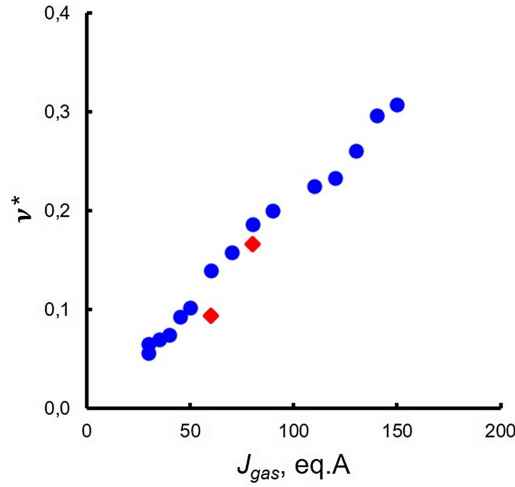


FIGURE 7. Collisionality in the transport section over the entire range of gas feeding. Blue, entrance of the transport part; red, exit of the transport section. The discharge power is 40 kW.

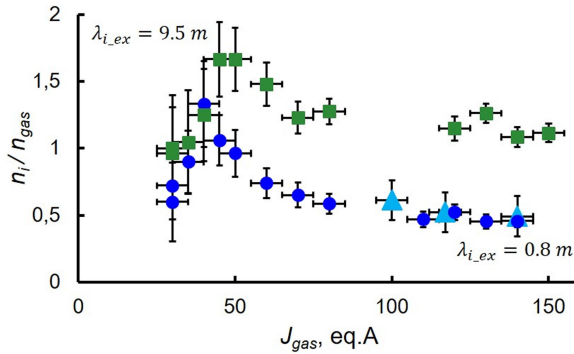


FIGURE 8. Plasma-gas density ratio in the confinement zone ($z = 0.4$ m). Dark blue circle, discharge power 20 kW; green square, 40 kW; blue triangle, experimental mode without floating diaphragms with 30 kW discharge power. Density is measured on the axis.

result led to regulation of the charge exchange scale (from $\lambda_{i,ex} = 0.8$ m to $\lambda_{i,ex} = 9.5$ m) in the confinement zone (figure 8) that influences the gas conditions in the transport section. Experimental plasma parameters in the entrance region of the transport section vary in limits:

$$\begin{aligned} n_i &= 2 \times 10^{18} \text{ m}^{-3}, \\ n_{\text{gas}} &= (1 \div 1.5) \times 10^{18} \text{ m}^{-3}, \\ T_e &= 20 \div 30 \text{ eV}, \quad T_i = 5 \div 7 \text{ eV}. \end{aligned}$$

The frequency of ion binary collisions prevails over the ion charge exchange (see table 1)

$$\frac{\nu_{ii}}{\nu_{i,ex}} = \frac{\lambda_{i,ex}}{\lambda_{ii}} \approx 2.4-10. \quad (3.5)$$

Process	Mean free path
Thermal molecule H_2 (500 K) relative to impact ionisation: $H_2 \rightarrow H^+ + H + e^-$	2–4 mm
Atom with energy 8 eV relative to impact ionisation	20–40 cm
Ion binary collision	0.5–3.3 m
Atom with energy 8 eV relative to charge exchange	2 m
Ion charge-exchange	5–8 m

TABLE 1. Mean free path of the most important processes.

This means that plasma friction of plasma against the gas is insignificant in the main experiments on studying plasma flow with low ion collisionality ν^* in the transport section of the SMOLA device.

4. Radial electric fields and current balance in the system

The effectiveness of helical plasma confinement in the SMOLA device is primarily determined by three interrelated parameters:

- (i) radial electric field E_r radial distribution, governs the $\mathbf{E} \times \mathbf{B}$ drift and consequent plasma rotation;
- (ii) angular rotation velocity $\omega_{E \times B}$, linear dependence with E_r ;
- (iii) axial mirror velocity in rotating frame V_Z , estimated via $\omega_{E \cdot B}$ and must satisfy $V_Z \geq V_{Ti}$ (ion thermal velocity) that is condition of effective helical confinement.

These parameters can be controlled through four adjustable features of the plasma source:

- (i) cathode, anode voltage;
- (ii) anode geometry;
- (iii) anode, ground potential (anode biasing);
- (iv) anode magnetic insulation.

4.1. The short anode mode

In the basic configuration of the source with the SA, only two parameters could be regulated: the cathode – anode voltage and the anode magnetic insulation. The anode in the SA mode was always grounded (see [figure 2](#)). In this mode, variation of the cathode anode voltage in the plasma gun was from 200 V to 300 V, the anode magnetic insulation as B_c/B_a ranged from 2 to 3.3.

Typical radial distributions of the electric potential and field in the SA mode measured by the double emissive probes are shown in [figure 9](#). Plasma in the confinement region has a negative potential on the axis ([figure 9a](#)), which leads to plasma pinching towards the axis (Sudnikov *et al.* 2020; Sudnikov *et al.* 2022a). In the straight-field mode, the plasma potential reaches $\varphi \approx (1.5 \div 3) \cdot T_e$ ([figure 9a](#)). Direct measurements of the potentials (in the same points on z and r) agree with the radial electric field profile. The radial electric field increases linearly from the plasma centre ($r = 0$ mm) to the edge (plasma SOL) in the core ($r = 50$ – 60 mm, see [figure 9b](#)). This plasma core is limited by the central diaphragm of the limiters.

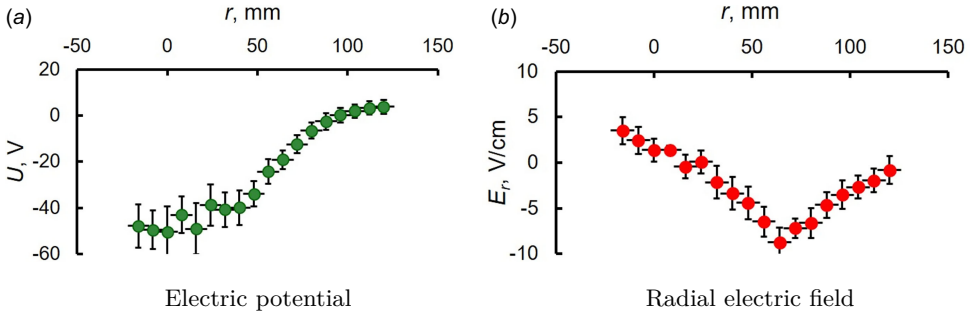


FIGURE 9. Radial distribution of the electric potential and the radial field in the plasma. Data are measured by the double emissive probe in the confinement zone ($z = 0.4$ m).

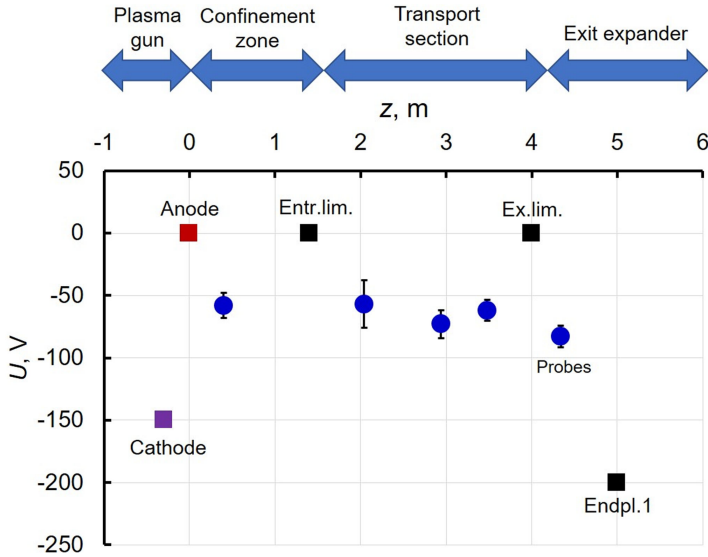


FIGURE 10. Axial distribution of the electric potential in the SMOLA device. Probes are located on the axis.

Thus, the plasma rotates with a constant radial angular velocity ω in the solid-state mode (with rigid core) along the device according with Doppler shift measurements (Inzhevatkina *et al.* 2021). In standard electric and gas feeding ($P_{\text{dis}} = 40$ kW and $J_{\text{gas}} = 50$ eq.A) of the plasma source with the SA, the plasma rotation velocity in the confinement region ($z = 1.15$ m) was $\omega = (0.8 \div 1.1) \times 10^6$ s $^{-1}$ (Inzhevatkina *et al.* 2021) at $B_c/B_a = 2.6$. The complex of the emissive probes allows one to measure the axial distribution of the radial profile of the plasma potential (figure 10), which was obtained relative to the material vacuum wall. The main potential variation at $\Delta\varphi \sim 100$ V is located between the cathode and the confinement zone ($z = 0.4$ m) and can be comparable with calculations according to the equality of the fluxes of ions and electrons to the wall $\Delta\varphi \sim (3-4) \cdot T_e/e$. In the rest of the facility along the magnetic field, the plasma potential changes insignificantly. This fact indicates that

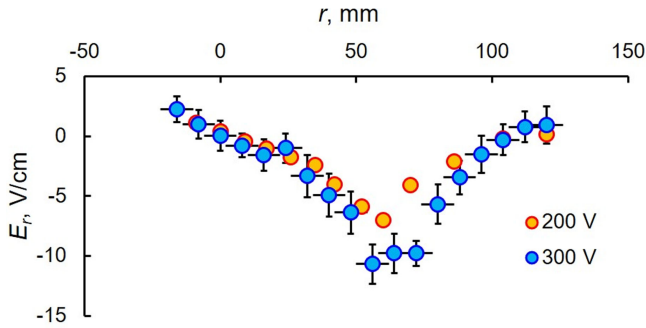


FIGURE 11. Radial electric field distribution at varied cathode potential. Data are measured at $z = 0.4$ m.

there is no significant thermal barrier between the transport section and the confinement zone. Double probes electron temperature measurements at $z = 0.4$ m and $z = 2.04$ m also confirm this fact.

In the grounded SA mode, variation of the cathode anode voltage in the plasma gun from 200 V to 300 V results in increasing of the electric field on the plasma core SOL border (figure 11); thus, extends the solid-state mode region. The angular rotational velocity of the rigid core was found to remain constant at the level of $\omega = (0.8 \div 1.1) \times 10^6 \text{ s}^{-1}$ when the rigid core expands. Thus, more plasma pieces can be rotated with the maximal velocity ω and trapped by magnetic mirrors that enhances the helical plasma confinement efficiency. The magnetic insulation of the anode does not influence the radial electric field distribution. The axial distribution of the potential saved after variation of the cathode–anode voltage in the plasma gun. Obtained results correspond to axial movement of the magnetic perturbations in the reference frame of rotating plasma $V_Z = h \cdot \omega_{E \times B} / (2\pi) = (2.9\text{--}3.4) \times 10^4 \text{ m s}^{-1}$, which is comparable and can be greater than the ion thermal velocity $V_{Ti} \sim 2 \times 10^4 \text{ m s}^{-1}$. Thus, the condition of the helical confinement $V_Z \geq V_{Ti}$ is satisfied and the efficiency of the longitudinal plasma flow suppression can be changed by the configuration of the plasma source (regulation of the rotation velocity).

4.2. The long anode mode

The anode's elongation by 3.5x (see figure 2) enhances the anode–plasma–cathode contact (the LA mode). This modification in the source leads to changes in the magnetic field configuration of the gun because the inner anode magnetic line needs to project on the cathode. In the LA mode, the inner anode magnetic line crosses only the cathode's edge that increases the anode's magnetic insulation and the electric resistance anode–cathode via the plasma. Such a change in the anode geometry can influence the currents in the system, radial electric field distribution and conditions of the stable discharge. In the experiments, the anode–ground voltage was varied and the anode's magnetic insulation was regulated. Variation of the anode–ground voltage (the anode biasing, U_{an}) in the plasma gun was from -200 V to 200 V, the anode magnetic insulation as B_c/B_a ranged from 1.15 to 1.7 in the LA mode experiments. The cathode–anode voltage stayed at a maximum value $U_{\text{cathode-anode}} = 300$ V.

Radial electric field in the plasma is evidence of the radial current existence in the plasma, which is a source of torque Ampere's force $j_r B_z$ that rotates the plasma

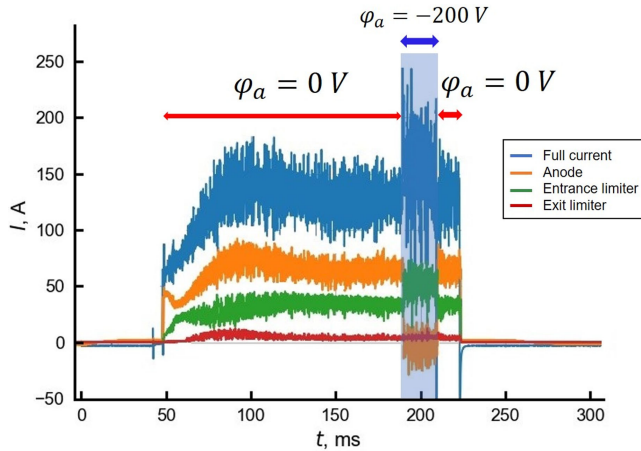


FIGURE 12. Dynamics of the currents in each electrode without the plasma dump in the modes with grounded LA and biasing LA. The limiters are grounded.

column in the SMOLA device. The current from the plasma to each electrode (or *vice versa*) can have a radial component. In our measurements, the endplate's current does not have a radial current from the plasma. Thus, radial currents from the anode and limiters transfer torque Ampere's force for plasma rotation. In all experiments with the grounded anode (SA mode and LA mode), there is a current disparity in the SMOLA device (figure 12). In the grounded anode mode, only half of full current moves in the plasma via the anode, and approximately 50 % of the residual current's part is detected in the limiters. Thus, a significant part of the current can form behind the anode.

Variation of the anode biasing in the LA mode has led to current redistribution. In the negative biasing LA mode, the anode-plasma current is minimised, while only the limiters' currents are detected; moreover, this current is less than 50 % the full current (figure 12). Such results give an idea that the remaining radial current can be formed between the plasma and the grounded wall of the entrance expander (confinement zone) and the transport section. Thus, this additional current is also one of the sources of the torque Ampere's force for the plasma rotation because the limiters have a thin radial border with the plasma and cannot collect all the remaining current. In the positive biasing LA mode, the full discharge current becomes less stable and after $U_{an} \geq 100$ V, the discharge is extinguished. The full discharge current in the LA mode linearly reduces at anode biasing from negative to positive in any magnitude of the B_c/B_a (figure 13). This current behaviour might be caused by potential shielding effects of the anode on the outer plasma column. Thus, the main experiments with radial electric field regulation have been performed with the negative biasing LA mode and the grounded LA mode.

In the negative biasing LA mode, the plasma core–edge boundary was shifted outward by 15–20 mm (from $r = 80$ mm to $r = 95$ –100 mm, figure 14) compare with the grounded LA mode in the confinement zone. The radial electric field at the plasma SOL increased by a factor of 2–3 (from 0.5 to 1.5 kV m⁻¹). So, the negative biasing LA mode allows for better rotation of the plasma edge without changing the electric field in the solid-state core and more pieces of the plasma will be rotated

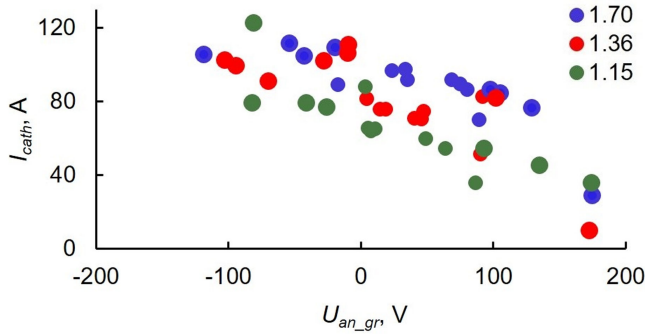


FIGURE 13. Discharge current at different anode biasing with regulated cathode–anode magnetic field ratio.

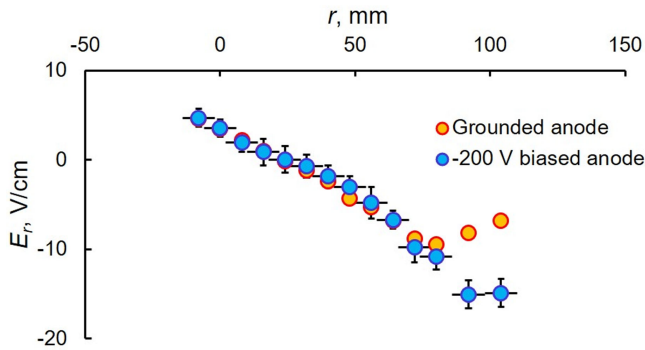


FIGURE 14. Radial distribution of the radial electric field in the LA mode with negative biasing and the grounded LA mode in the confinement zone ($z = 0.4$ m).

with the maximal angular rotation velocity ω . The anode's magnetic insulation also affects the radial electric field in the negative biasing LA mode (figure 15). Reducing the anode magnetic insulation (increasing contact surface of the LA with the cathode), the radial electric field can also be increased by a factor of 3 in the plasma SOL at negative anode biasing. At the same time, Doppler spectroscopy measured similar values of the angular rotational velocity $\omega \leq 1.1 \times 10^6 \text{ s}^{-1}$ as the grounded SA mode. As a result, the condition of the helical confinement $V_z \geq V_{Ti}$ is satisfied in the LA mode saving the scale of the V_z . The restriction of ω may be related to the Kelvin–Helmholtz instability on the border between rigid core and SOL (Beklemishev 2024).

5. Summary

The experiments discussed in this paper have demonstrated effective control over plasma formation, collisionality and rotation in the SMOLA device through optimised configuration of the plasma source. Key findings are summarised here.

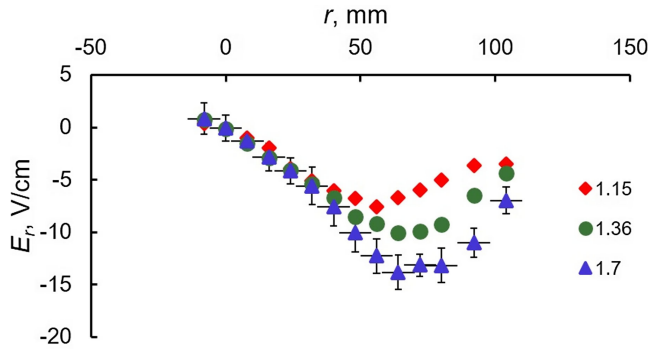


FIGURE 15. Radial distribution of the radial electric field in the LA mode with negative biasing (example radial profile at $U_{\text{an}} = -80$ V) and different anode's magnetic insulation in the confinement zone ($z = 0.4$ m).

(i) Plasma Source Performance

- (a) The axisymmetric plasma gun with LaB_6 cathode and elongate copper anode successfully generated stable rotating plasma flow with densities up to 10^{19} m^{-3} and adjustable collisionality.
- (b) Installation of floating diaphragms improved gas efficiency, enabling operation at lower gas feed rates (down to 50 eq.A) while maintaining linear density scaling at discharge power more than 30 kW.
- (c) Adjustment of the anode magnetic insulation ($B_c/B_a = 1.15\text{--}3.3$) influences the gas efficiency, reducing plasma density and increasing neutrals density at smaller the anode magnetic field.

(ii) Control of ion collisionality

- (a) Ion collision regimes in the transport section were turned from collisional to collisionless ($\lambda/h \sim 0.3\text{--}12$) via gas feed regulation.
- (b) Ion-ion binary collisions dominated over charge-exchange ($\nu_{ii}/\nu_{i,\text{ex}} \approx 2.4\text{--}10$), minimising neutral gas friction effects.

(iii) Radial electric field and rotation dynamics

(a) Short Anode (SA) Mode (grounded):

- (i) linear E_r profile in the plasma core ($r = 0\text{--}60$ mm), but limited the edge control;
- (ii) achieved rigid-core rotation with the angular rotation velocity $\omega \leq 1.1 \times 10^6 \text{ s}^{-1}$ and $V_z \geq V_{Ti}$.

(b) Long Anode (LA) Mode (biased):

- (i) negative anode bias (-200 V) enhanced E_r at the plasma SOL by 2–3 (up to 1.5 kV m^{-1}) in the confinement zone;

- (ii) expanded rotation region of the rigid-core while maintaining $\omega \leq 1.1 \times 10^6 \text{ s}^{-1}$ (the Kelvin–Helmholtz instability) and $V_z \geq V_{Ti}$;
- (iii) positive bias at $U_{an} \geq 100 \text{ V}$ caused the discharge instability.
- (iv) Current distribution
 - (a) Torque from Ampere's forces $j_r B_z$ sustained plasma rotation along the SMOLA device.
 - (b) Current disparity:
 - (i) grounded anode: half of the full current via the anode, 20–30 % to the limiters;
 - (ii) negative anode bias: current shifted to limiters and chamber walls and there was not current via the anode.

The modified plasma source performs tasks for effective helical confinement investigations on the SMOLA device for the new generation magnetic mirror device – the GDMT project.

Acknowledgements

All authors contributed equally to analysing data and reaching conclusions, and in writing the paper. The authors thank Dr. A. Beklemishev and Professor V. Davydenko for valuable discussions.

Editor Cary Forest thanks the referees for their advice in evaluating this article.

Funding

This research received no specific grant from any funding agency, commercial or not-for-profit sectors.

Declaration of interests

The authors report no conflict of interest.

REFERENCES

- AKHMETOV, T.D., DAVYDENKO, V.I., IVANOV, A.A. & SHULZHENKO, G.I. 2019 Operation modes of hot-cathode plasma source for linear devices. *Plasma and Fus. Res.* **14**, 2406004.
- AKHMETOV, T.D., DAVYDENKO, V.I., IVANOV, A.A., KRETER, A., MISHAGIN, V.V., SAVKIN, V.YA., SHULZHENKO, G.I. & UNTERBERG, B. 2016 Arc discharge plasma source with plane segmented laB_6 cathode. *Rev. Sci. Instrum.* **87**, 056106.
- ANIKEEV, A.V., *et al.* 2015 Small-scale variation of convected quantities like temperature in turbulent fluid. Part 1. General discussion and the case of small conductivity. *Materials* **8**, 84528459.
- BEKLEMISHEV, A.D. 2013 Helicoidal system for axial plasma pumping in linear traps. *Fusion Sci. Technol.* **63**, 355–357.
- BEKLEMISHEV, A.D. 2015 Helical plasma thruster. *Phys. Plasmas* **22**, 103506.
- BEKLEMISHEV, A.D. 2016 Radial and axial transport in trap sections with helical corrugation. *AIP Conf. Proc.* **1771**, 040006.
- BEKLEMISHEV, A.D. 2024 Plasma rotation induced by biasing in axially symmetric mirrors. *J. Plasma Phys.* **90**, 975900601.
- CHERNOSHTANOV, I.S. & AYUPOV, D.A. 2021 Collisionless particle dynamics in trap sections with helical corrugation. *Phys. Plasmas* **28**, 032502.

- FOREST, C.B., *et al.* 2024 Prospects for a high-field, compact break-even axisymmetric mirror (beam) and applications. *J. Plasma Phys.* **90**, 975900101.
- GOEBEL, D.M., HIROOKA, Y. & SKETCHLEY, T.A. 1985 Large area lanthanum hexaboride electron emitter. *Rev. Sci. Instrum.* **56**, 1717–1722.
- GOTA, H., BINDERBAUER, M.W., TAJIMA, T., PUTVINSKI, S., TUSZEWSKI, M., DENG, B.H. & DETTRICK, S.A. 2019 Formation of hot, stable, long-lived field-reversed configuration plasmas on the C-2W device. *Nucl. Fusion* **59**, 11.
- HERSHKOWITZ, N., NELSON, B., PEW, J. & GATES, D. 1983 Self-emissive probes. *Rev. Sci. Instrum.* **54**, 29–34.
- INZHEVATKINA, A.A., BURDAKOV, A., IVANOV, I., LOMOV, K.A., POSTUPAEV, V., SUDNIKOV, A. & USTYUZHANIN, V.O. 2021 Investigation of the plasma rotation in SMOLA helical mirror. *Plasma Phys. Rep.* **47**, 794–802.
- IVANOV, I.A., USTYUZHANIN, V.O., SUDNIKOV, A.V. & INZHEVATKINA, A.A. 2021 Long-pulse plasma source for SMOLA helical mirror. *J. Plasma Phys.* **87**, 845870201.
- JÄDERBERG, J., SCHEFFEL, J., BENDTZ, K., HOLMBERG, R., LINDVALL, K., NIVA, P., DAHLBÄCK, R. & DUNNE, K. 2023 Introducing the novatron, a novel reactor concept. arXiv: 2310.16711.
- KRETER, A., BRANDT, C., HUBER, A., KRAUS, S., MÖLLER, S., REINHART, M., SCHWEER, B., SERGIENKO, G. & UNTERBERG, B. 2017 Linear plasma device PSI-2 for plasma-material interaction studies. *Fusion Sci. Technol.* **68**, 8–14.
- POSTUPAEV, V.V., BATKIN, V.I., BEKLEMISHEV, A.D., BURDAKOV, A.V., BURMASOV, V.S., CHERNOSHANOV, I.S., GORBOVSKY, A.I., IVANOV, I.A., KUKLIN, K.N. & MEKLER, K.I. 2017 The GOL-NB program: further steps in multiple-mirror confinement research. *Nucl. Fusion* **57**, 14.
- SKOVORODIN, D.I., *et al.* 2023 Gas-dynamic multi-mirror trap gdmr. *Plasma Phys. Rep.* **49**, 1039–1086.
- SUDNIKOV, A.V., BEKLEMISHEV, A.D., POSTUPAEV, V.V., BURDAKOV, A.V., IVANOV, I.A., VASILYEVA, N.G., KUKLIN, K.N. & SIDOROV, E.N. 2017 SMOLA device for helical mirror concept exploration. *Fusion Engng Des.* **122**, 86–93.
- SUDNIKOV, A.V., BEKLEMISHEV, A.D., POSTUPAEV, V.V., IVANOV, I.A., INZHEVATKINA, A.A., SKLYAROV, V.F., BURDAKOV, A.V., KUKLIN, K.N., ROVENSKIKH, A.F. & MELNIKOV, N.A. 2019 First experimental campaign on SMOLA helical mirror. *Plasma Fusion Res.* **14**, 4.
- SUDNIKOV, A.V., BEKLEMISHEV, A.D., INZHEVATKINA, A.A., IVANOV, I.A., POSTUPAEV, V.V., BURDAKOV, A.V., GLINSKIY, V.V., KUKLIN, K.N., ROVENSKIKH, A.F. & USTYUZHANIN, V.O. 2020 Preliminary experimental scaling of the helical mirror confinement effectiveness. *J. Plasma Phys.* **86**, 14.
- SUDNIKOV, A.V., IVANOV, I.A., INZHEVATKINA, A.A., LARICHKIN, M.V., LOMOV, K.A., POSTUPAEV, V.V., TOLKACHEV, M.S. & USTYUZHANIN, V.O. 2022a Plasma flow suppression by the linear helical mirror system. *J. Plasma Phys.* **88**, 905880102.
- SUDNIKOV, A.V., IVANOV, I.A., INZHEVATKINA, A.A., LARICHKIN, M.V., POSTUPAEV, V.V., SKLYAROV, V.F., TOLKACHEV, M.S. & USTYUZHANIN, V.O. 2022b Helical magnetic mirror performance at up- and downstream directions of the axial force. *J. Plasma Phys.* **88**, 905880609.
- YAKOVLEV, D., CHEN, Z., BAGRYANSKY, P., BRAGIN, A., KOTELNIKOV, I., KUZMIN, E., PRIKHODKO, V., SHIKHOVTSEV, I., USOV, P. & WANG, Z. 2022 Conceptual design of the ALIANCE-t mirror experiment. *Nucl. Fusion* **62**, 076017.